energy&fuels

Article

Cite This: Energy Fuels XXXX, XXX, XXX−XXX

pubs.acs.org/EF

# $\alpha$-$Fe_2O_3$ Nanoparticles as Oxygen Carriers for Chemical Looping Combustion: An Integrated Materials Characterization Approach to Understanding Oxygen Carrier Performance, Reduction Mechanism, and Particle Size Effects

Hayder A. Alalwan,[†,‡] Sara E. Mason,[§] Vicki H. Grassian,*[,†,§,∥] and David M. Cwiertny*[,†,⊥]

[†]Department of Chemical and Biochemical Engineering, University of Iowa, Iowa City, Iowa 52242, United States

[‡]Kut Technical Institute, Middle Technical University, Kut, Wasit, Iraq

[§]Department of Chemistry, University of Iowa, Iowa City, Iowa 52242, United States

[∥]Departments of Chemistry and Biochemistry, Nanoengineering, and Scripps Institution of Oceanography, University of California San Diego, La Jolla, California 92093, United States

[⊥]Department of Civil and Environmental Engineering, University of Iowa, Iowa City, Iowa 52242, United States

Supporting Information

**ABSTRACT:** Through continuous flow reactor experiments, materials characterization, and theoretical calculations, we provide new insights into the reduction of hematite ($\alpha$-$Fe_2O_3$) nanoparticles by methane ($CH_4$) during chemical looping combustion (CLC). Across CLC-relevant temperatures (500−800 °C) and gas flow rates (2.5−250 $h^{-1}$), decreasing $\alpha$-$Fe_2O_3$ particle size (from 350 to 3 nm) increased the duration over which $CH_4$ was completely converted to $CO_2$ (i.e., 100% yield). We attribute this size-dependent performance trend to the greater availability of lattice oxygen atoms in the near-surface region of smaller particles with higher surface area-to-volume ratios. All particle sizes then exhibited a relatively rapid rate of reactivity loss that was size- and temperature-independent, reflecting a greater role for magnetite ($Fe_3O_4$), the primary $\alpha$-$Fe_2O_3$ reduction product, in $CH_4$ oxidation. Bulk (X-ray diffraction, XRD) and surface (X-ray photoelectron spectroscopy, XPS) analysis revealed that oxygen carrier reduction proceeds via a two-stage solid-state mechanism; $\alpha$-$Fe_2O_3$ reduction to $Fe_3O_4$ followed the unreacted shrinking core model (USCM) while subsequent reduction of $Fe_3O_4$ to wüstite (FeO) and FeO to iron metal (Fe) followed the nucleation and nuclei growth model (NNGM). Atomistic thermodynamics modeling based on density functional theory supports that reduction initiates via the USCM, as partially reduced $\alpha$-$Fe_2O_3$ surfaces exhibited a wide range of stability relative to bulk $Fe_3O_4$. Reduction and reoxidation cycling experiments were also performed to explore more practical aspects related to the long-term performance of unsupported $\alpha$-$Fe_2O_3$ nanoparticles as oxygen carriers for CLC.

## 1. INTRODUCTION

The combustion of natural gas and other fossil fuels is the main source of greenhouse gases, which contribute to global warming. Among those gases, $CO_2$ has the highest impact on the environment, and thus, approaches to minimize its formation and release are a priority.[1] Chemical looping combustion (CLC) is a promising indirect combustion process that facilitates capture of $CO_2$. CLC uses solid-state oxygen carriers to combust hydrocarbon fuels, thereby avoiding direct contact between the fuel and air and the associated formation of unwanted combustion by-products (e.g., $NO_x$).

Low in cost and naturally abundant, $\alpha$-$Fe_2O_3$ is a promising oxygen carrier not only for CLC[2−6] but also for processes such as chemical looping reforming (CLR) and syngas chemical looping (SCL) gasification, all of which use two separate reactors.[7−9] One reactor is used to combust the hydrocarbon fuel by utilizing the lattice oxygen of the oxygen carrier, while the other reactor is used to regenerate the spent (i.e., reduced) oxygen carrier via oxidation in air. For these processes, $\alpha$-$Fe_2O_3$ is especially desirable because it possesses the highest theoretical oxygen capacity among transition metal oxides commonly considered for CLC at 30.1% (wt),[10] assuming complete reduction to Fe via $Fe_3O_4$ and FeO (e.g., see hematite stability diagram as a function of temperature and oxygen pressure in the paper by Ketteler and co-workers[11]).

For CLC, the thermodynamically favorable reduction of $\alpha$-$Fe_2O_3$ to $Fe_3O_4$ results in the corresponding release of lattice oxygen to drive the complete oxidation of $CH_4$, which is the primary component of natural gas (eq 1).[10] The continued reduction of $Fe_3O_4$ to FeO or metallic iron (Fe) is slower and can lead to the partial oxidation of $CH_4$, a process that yields carbon monoxide (CO) and hydrogen gas ($H_2$) as by-products (eq 2).[12−15]

$$CH_4 + 2O_2 \leftrightarrow CO_2 + 2H_2O \quad (1)$$

$$CH_4 + 1/2O_2 \leftrightarrow CO + 2H_2 \quad (2)$$

The formation of CO and $H_2$ are undesirable in CLC, which aims to eliminate gaseous by-products so as to achieve a pure

Received: May 2, 2018
Revised: June 12, 2018
Published: June 17, 2018






DOI: 10.1021/acs.energyfuels.8b01539
Energy Fuels XXXX, XXX, XXX−XXX

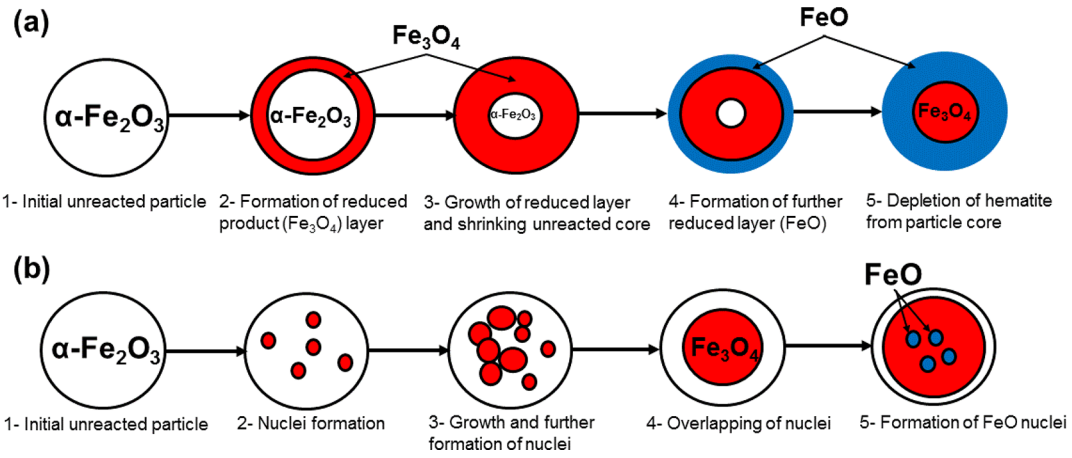


**Figure 1.** Two proposed models for the reduction of $\alpha$-$Fe_2O_3$ during CLC. These are (a) the unreacted shrinking core model (USCM) and (b) the nucleation and nuclei growth model (NNGM).

stream of $CO_2$ that is easier for capture. In contrast, $H_2$ is the desired product in CLR and SCL.

$\alpha$-$Fe_2O_3$ reduction has been described in the literature by two general models: an unreacted shrinking core model (USCM)[16] and a nucleation and nuclei growth model (NNGM)[17,18] (Figure 1). According to the unreacted shrinking core model, consumption of lattice oxygen from the surface creates a layer of reduced metal/metal oxide that gaseous reactants and products must then diffuse through for sustained reactivity.[19] As the reaction proceeds, this interface between the outer reduced phase and the inner oxidized phase migrates toward the core of the oxygen carrier particle. As such, the heterogeneous reaction between $CH_4$ and $\alpha$-$Fe_2O_3$ proceeds via three steps, external mass transfer, internal mass transfer, and chemical reaction (e.g., electron or oxygen transfer), any of which may be rate limiting. Notably, Briggs and Sacco[20] concluded that the reduction mechanism is partially controlled by the chemical reaction at the interface and partially by gas transport through the solid product.

In contrast, the nucleation and nuclei growth model assumes that the first step in the reduction reaction is nuclei formation of the new reduced phase. Subsequently, the reaction progresses more quickly with a random distribution of nuclei or product phases due to oxygen vacancy formation, which promotes the release of more bulk oxygen molecules.[21] In our previous study of the reduction of cobalt oxides by $CH_4$,[22] we observed evidence for such a mechanism; during reduction of CoO, the formation of Co metal sped up the release of lattice oxygen from CoO, a behavior we attributed to the oxygen vacancies generated via CoO reduction (or Co metal formation).[22] Previously, some have suggested a similar mechanism may be at play for $\alpha$-$Fe_2O_3$ reduction. Monazam and co-workers[23,24] proposed a multistep mechanism for $\alpha$-$Fe_2O_3$ reduction to FeO, with the first step involving $\alpha$-$Fe_2O_3$ reduction to $Fe_3O_4$ (by either $H_2$ or $CH_4$) via the USCM and the second step involving the subsequent reduction of $Fe_3O_4$ to FeO via the NNGM.

Additionally, an important material property recognized to influence the rate and mechanism of $\alpha$-$Fe_2O_3$ reduction is particle size.[25] To date, however, particle size as a key operational variable for the application of $\alpha$-$Fe_2O_3$ as an oxygen carrier has not been closely examined, especially for nanoparticles with a primary particle size below 100 nm in diameter. Recent investigations have revealed that using nanoparticles instead of more conventional, larger millimeter- or micrometer-sized particles may hold several advantages for performance, including increasing reactivity, decreasing mass resistance, and promoting heat transfer, which facilitates oxygen carrier performance at lower temperatures.[26−28] Most previous studies have focused on $\alpha$-$Fe_2O_3$ particle sizes ranging from micrometers to millimeters and have found that decreasing particle size leads to an increase in the rate of $\alpha$-$Fe_2O_3$ reduction and a decrease in the temperature required for the reduction reaction to proceed.[29,30] For example, Pang and co-workers[29] found that a decrease in $\alpha$-$Fe_2O_3$ particle size from ∼100 to 2 $\mu$m led to a reduction in the activation energy necessary for $\alpha$-$Fe_2O_3$ reduction by $H_2$ from 78.3 to 36.9 kJ/mol across a temperature range from 450 to 600 °C. These results illustrate the promise of tailoring $\alpha$-$Fe_2O_3$ particle size to further improve process efficiency.

In this study, a set of unsupported $\alpha$-$Fe_2O_3$ nanoparticles (nominally 3, 50, and 350 nm in diameter) was used to explore the influence of particle size on the reactivity of $\alpha$-$Fe_2O_3$ toward $CH_4$. While we acknowledge the practical concerns associated with use of unsupported nanoparticles for CLC (e.g., agglomeration), they represent the best option for studying the inherent reactivity and solid-state reduction mechanism of oxygen carriers without influence from the underlying support material. Using a continuous flow reactor with gas chromatography (GC) analysis, we report size-dependent trends for the performance of $\alpha$-$Fe_2O_3$ nanoparticles across a range of temperatures (500−800 °C) and flow rates (2−40 standard cubic centimeters or sccm) relevant to the CLC process. Through complementary measurements of $CH_4$ conversion efficiency, characterization of $\alpha$-$Fe_2O_3$ bulk and surface properties, and atomistic thermodynamics modeling based on density functional theory, we also provide an improved understanding of the solid-state reduction mechanism of $\alpha$-$Fe_2O_3$ by $CH_4$. Collectively, our results provide new insights that will help to establish the viability of $\alpha$-$Fe_2O_3$ nanoparticles as solid-state oxygen carriers while also identifying the operational parameters optimal for their performance in CLC.

## 2. EXPERIMENTAL SECTION

**2.1. Materials and Reagents.** Differently sized nanoparticles of $\alpha$-$Fe_2O_3$ were acquired from commercial vendors. Nominal vendor-reported average particles sizes were 3 nm (Alfa Aesar, purity


DOI: 10.1021/acs.energyfuels.8b01539
Energy Fuels XXXX, XXX, XXX−XXX

99.95%), 30−50 nm (Nanostructure & Amorphous Materials, purity 99%), and <1 μm (Sigma-Aldrich, purity 99+%). A mixture (P5 gas, Praxair) of $CH_4$ (5%) in balance with argon (95%) was used to reduce the $\alpha$-$Fe_2O_3$ oxygen carrier during CLC experiments, and synthetic air (Praxair) was used during the preheating portion of our protocol as well as in reoxidation of the oxygen carrier to test its performance and stability through multiple cycles. High purity nitrogen (Praxair, 99.9%) was used to flush the reactor of air prior to the introduction of P5 to initiate the reaction.

**2.2. Characterization of Oxygen Carriers.** To evaluate changes in the $\alpha$-$Fe_2O_3$ structure and phase during the reduction process, particles were examined before, during, and after reaction with $CH_4$ using a suite of characterization techniques. X-ray diffraction (XRD, Bruker D8 Advance 206112) analysis was used to identify the bulk crystalline phase present before, during, and after reaction of $\alpha$-$Fe_2O_3$ nanoparticles with $CH_4$. X-ray photoelectron spectroscopy (XPS) analysis provided information about how the surface composition of particles evolved during the reaction. The surface analysis chamber of the XPS instrument (Kratos Axis Ultra XPS) was equipped with an aluminum K$\alpha$ source with a 500 mm Rowland circle silicon single-crystal monochromator that produces a monochromatic X-ray beam of 1486.6 eV. The X-ray gun was operated using a 10 mA emission current at an accelerating voltage of 15 kV. XPS spectra of $\alpha$-$Fe_2O_3$ were calibrated using the adventitious C 1s peak at 285.0 eV. High-resolution transmission electron microscopy (HRTEM, JEOL 2100F) with an accelerating voltage of 200 kV was used to determine particle size distributions of $\alpha$-$Fe_2O_3$ samples by measuring at least 125 randomly chosen particles. HRTEM samples were prepared after sonication of nanoparticle suspensions in water for 20 min at room temperature. Scanning electron microscopy (SEM, Hitachi S-4800) was used to examine the <1 μm sample, as the relatively large size of the particles precluded HRTEM analysis. Samples were imaged on an Au-coated silicon wafer, and the particle size distribution was once again determined by measuring at least 125 randomly chosen particles of this sample. The specific surface area of all unreacted (i.e., as-received) samples was determined using the Brunauer−Emmett−Teller (BET) adsorption isotherm method, in which particles were first degassed for 3 h at 110 °C. A seven-point BET isotherm was used to determine the specific surface area using $N_2$ (g) as the adsorbate on a Quantachrome Nova 4200e Surface Area and Pore Size Analyzer.

**2.3. Reactor Operation and Effluent Gas Sampling.** To examine the performance of $\alpha$-$Fe_2O_3$ as an oxygen carrier for CLC, reactions with $CH_4$ were conducted in a tube furnace (Thermolyne, type 21100−15 in. long) fitted with a quartz tube reactor (3/8 in. in diameter, and 18 in. long; see Figure S1 in the Supporting Information). The reactor inlet was connected to a three-way valve, which allowed control of the inlet gas composition. We previously used this setup in an investigation of cobalt oxides as oxygen carriers for CLC.[22]

Reactions between $\alpha$-$Fe_2O_3$ and $CH_4$ were investigated as a function of gas hourly space velocity (GHSV) and temperature. Gases were introduced into the reactor using mass flow controllers (MKS) with a range up to 100 standard cubic centimeters per minute (sccm). P5 gas was used at a flow rate between 2 and 40 sccm, and the typical metal oxide loading in the reactor was one gram. These conditions produced GHSV values between 12.5 and 250 $h^{-1}$, where values were calculated based on the volumetric $CH_4$ flow rate normalized to the reactor bed volume (i.e., the volume of $\alpha$-$Fe_2O_3$). The reaction temperatures investigated were in the range of 500−800 °C.

To initiate an experiment, the tube reactor was filled with $\alpha$-$Fe_2O_3$ and then heated to the desired temperature under a stream of air or nitrogen (60 sccm). When the desired temperature was achieved, the air flow was stopped and $N_2$ was introduced at the same flow rate for 5 min prior to introducing the P5 gas to eliminate the air from the reactor. Upon introduction of P5, samples were taken periodically for gas chromatography (GC) analysis to monitor the concentration of $CH_4$, $CO_2$, and other potential reaction by-products (e.g., CO and $H_2$) in the reactor effluent. For sample collection, the reactor outlet was connected to a three-way valve with one port sealed by septa, from which a gas-tight needle (250 μL) was used to extract a sample of the reaction gas products. Gas samples were collected every 5 min. When samples of the reacted oxygen carrier were needed to examine changes in morphology and composition along the reaction coordinate, the reactor was cooled under an $N_2$ stream, and the samples were stored under vacuum until analysis. Each set of experiments was conducted at least twice, and good reproducibility was generally observed.

**2.4. Long-Term $\alpha$-$Fe_2O_3$ Performance through Simulated CLC Cycling.** The long-term performance of the three unsupported $\alpha$-$Fe_2O_3$ samples as oxygen carriers during $CH_4$ oxidation was also investigated. These stability experiments were conducted at a reaction temperature of 600 °C and with P5 gas at a flow rate of 20 sccm (GHSV = 125 $h^{-1}$). These conditions were chosen because all samples exhibited an initial reactivity of at least 90% conversion of $CH_4$ to $CO_2$ that was sustained over the first 5 min of reactor operation. After the first reaction step, which was conducted for 5 min, the oxygen carriers were processed via repeated oxidation (by air) and reduction (by $CH_4$) cycling to simulate their application in CLC. This cycle involved reoxidation of reacted carriers by air at a flow rate of 60 sccm and their subsequent reduction by P5 gas for 5 min, after which the oxidation and reduction cycle was repeated ten times. We note that prior to reintroducing P5 to the reactor to initiate the next reduction/reoxidation cycle, $N_2$ was passed through the reactor at a flow rate of 60 sccm for 2 min, which was sufficient to remove any of residual reactant or product gases from the system.

**2.5. Gas Chromatography.** Effluent gas analysis was performed using an Agilent 6890N Network Gas Chromatograph (GC) equipped with a thermal conductivity detector (TCD) and Porpak Q packed column (Alltech). The column dimension was 4 m (length) × 1/8″ (diameter) × 0.085″ (film thickness). Helium (He) was used as a carrier gas. GC temperatures were set at 200, 40, and 225 °C for the inlet, column, and detector, respectively. Pure samples (99.99+%, Matheson) of $CH_4$, $CO_2$, CO, and $H_2$ were used as standards.

**2.6. Density Functional Theory Calculations and Thermodynamics Modeling.** Spin-polarized density functional theory (DFT) calculations were carried out using the QUANTUM-ESPRESSO package,[31] employing the GGA-PBE approximation to the exchange-correlation functional.[32] The periodic boundary condition calculations were carried out using ultrasoft pseudopotentials[33] and planewave cutoffs of 35 Ry for the wave function and 280 Ry for the charge density. The energy of bulk $\alpha$-$Fe_2O_3$ modeled in a rhombohedral primitive cell was sampled using an 8 × 8 × 8 k-point mesh,[34] which was subsequently folded down to 4 × 4 × 1 and 2 × 2 × 1 for (1 × 1) and (2 × 2) supercells of the (001) surface plane, respectively. Additional details of the computational methods, including the optimized lattice constants, Hubbard $U$ corrections applied to the 3d and 2p states of Fe and O atoms, respectively, surface slab thickness convergence studies, and magnetic ordering, have been previously reported.[35] Surface slabs were constructed to contain inversion symmetry, and all atoms were allowed to fully relax over the course of geometry optimizations carried out to within convergence criteria of $10^{-3}$ eV and a residual force of $10^{-2}$ eV/ Å per atom.

The stability of different $FeO_x$ species was examined using atomistic thermodynamics modeling that uses DFT total energy information and as described originally by Reuter and Scheffler.[36−38] Our calculated surface free energies are consistent with those of other ab initio thermodynamics studies of $\alpha$-$Fe_2O_3$(001) surfaces modeled using different implementations of DFT.[39,40]

## 3. RESULTS AND DISCUSSION

**3.1. Characterizations of Oxygen Carriers.** From HRTEM and SEM analyses, the average projected area diameter (i.e., a two-dimensional area measurement of particle TEM images obtained by projecting their shapes onto an arbitrary plane) of the three $\alpha$-$Fe_2O_3$ nanoparticle samples before reaction (as-received) were found to be 3 (± 0.5), 50 (± 17), and 350 (± 150) nm (see Figure S2). Hereafter, for simplicity, we refer to our samples as 3, 50, 350 nm. The


DOI: 10.1021/acs.energyfuels.8b01539
Energy Fuels XXXX, XXX, XXX−XXX

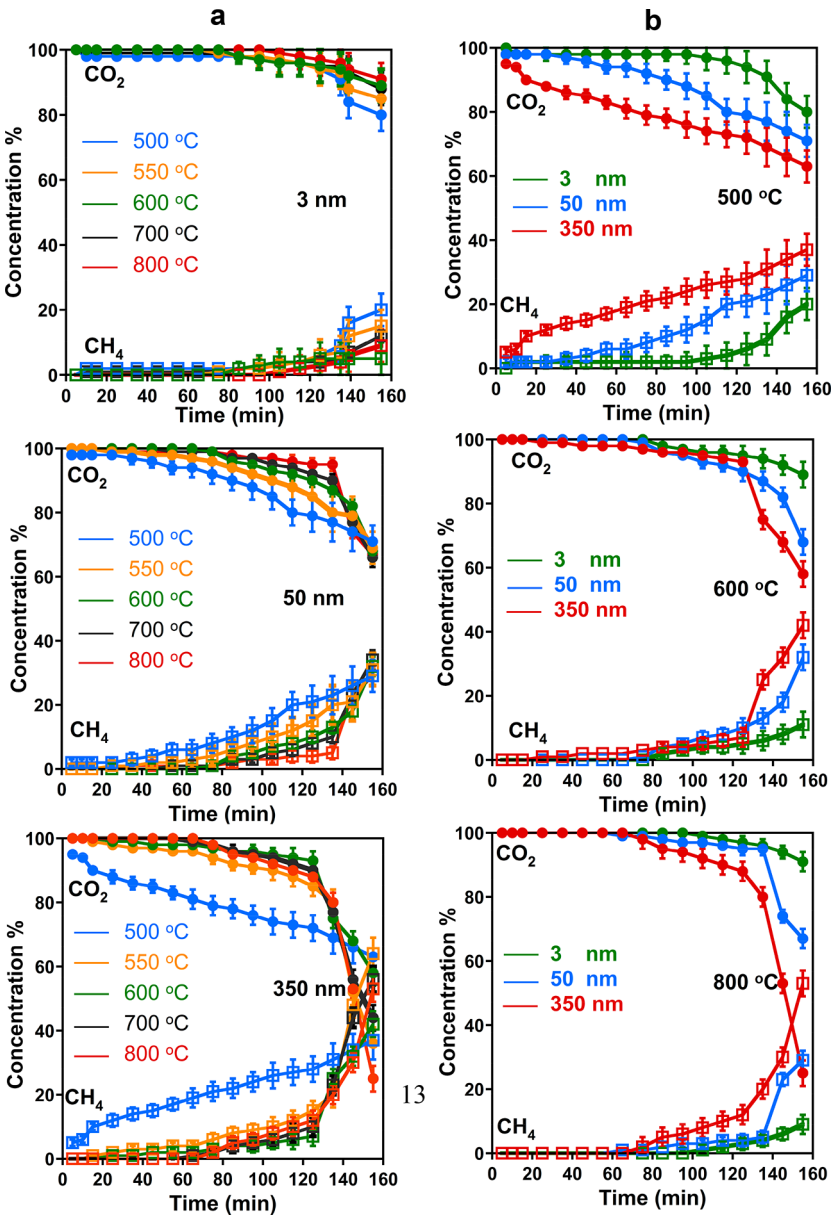


**Figure 2.** Effect of (a) temperature (500−800 °C) at a fixed particle size and (b) particle size at a fixed temperature for $\alpha$-$Fe_2O_3$ oxidation of $CH_4$ (present at 5% in a standard P5 gas mixture) to $CO_2$ at a flow rate of 2 sccm (12.5 $h^{-1}$ as GHSV). Results from at least duplicate reactions are shown (as averages with standard deviation) for all concentration data.

specific surface areas of as-received 3, 50, and 350 nm $\alpha$-$Fe_2O_3$ particles were 190 (± 25), 24 (± 1), and 4.0 (± 0.5) $m^2/g$, respectively, where values represent the average and standard deviation from triplicate measurements. As expected, the specific surface area of the particles decreased with increasing primary particle size. The XRD pattern of all as-received $\alpha$-$Fe_2O_3$ samples (Figure S3) matched that of a trigonal hexagonal $\alpha$-$Fe_2O_3$ phase with the rhombohedral lattice system (JCPDS card 01-076-9683). The XRD diffraction pattern of the as-received 3 nm sample revealed it was initially poorly crystalline, but upon heating under an air stream to the reaction temperatures typical for CLC (500−800 °C), the material developed better crystallinity.

**3.2. Temperature-Dependent Trends in $CH_4$ Oxidation by Nanoscale $\alpha$-$Fe_2O_3$.** Figure 2a shows the effect of temperature (500−800 °C) on the oxidation of $CH_4$ (present at 5% in a standard P5 gas mixture) to $CO_2$ at a flow rate of 2 sccm (12.5 $h^{-1}$ as GHSV) for different $\alpha$-$Fe_2O_3$ particle sizes. Data are shown as a function of temperature for each particle size (Figure 2a) and also as a function of particle size at each of the different temperatures (Figure 2b).

Generally, and as we also observed previously for cobalt oxides,[22] conversion of $CH_4$ to $CO_2$ was most efficient (i.e., producing the highest $CO_2$ yield over the longest durations) at higher temperatures. Also, the performance of the oxygen carrier was clearly influenced by particle size (Figure 2b). For example, 3 nm particles at 500 °C facilitated complete $CH_4$ conversion to $CO_2$ (i.e., 100% $CO_2$ yield) over nearly 120 min. In contrast, we never observed 100% conversion of $CH_4$ conversion to $CO_2$ for 350 nm particles at this same temperature. More sustained periods of higher $CO_2$ yield were also observed for smaller $\alpha$-$Fe_2O_3$ particles at the other temperatures tested (as shown in Figure 2b).



DOI: 10.1021/acs.energyfuels.8b01539
Energy Fuels XXXX, XXX, XXX−XXX

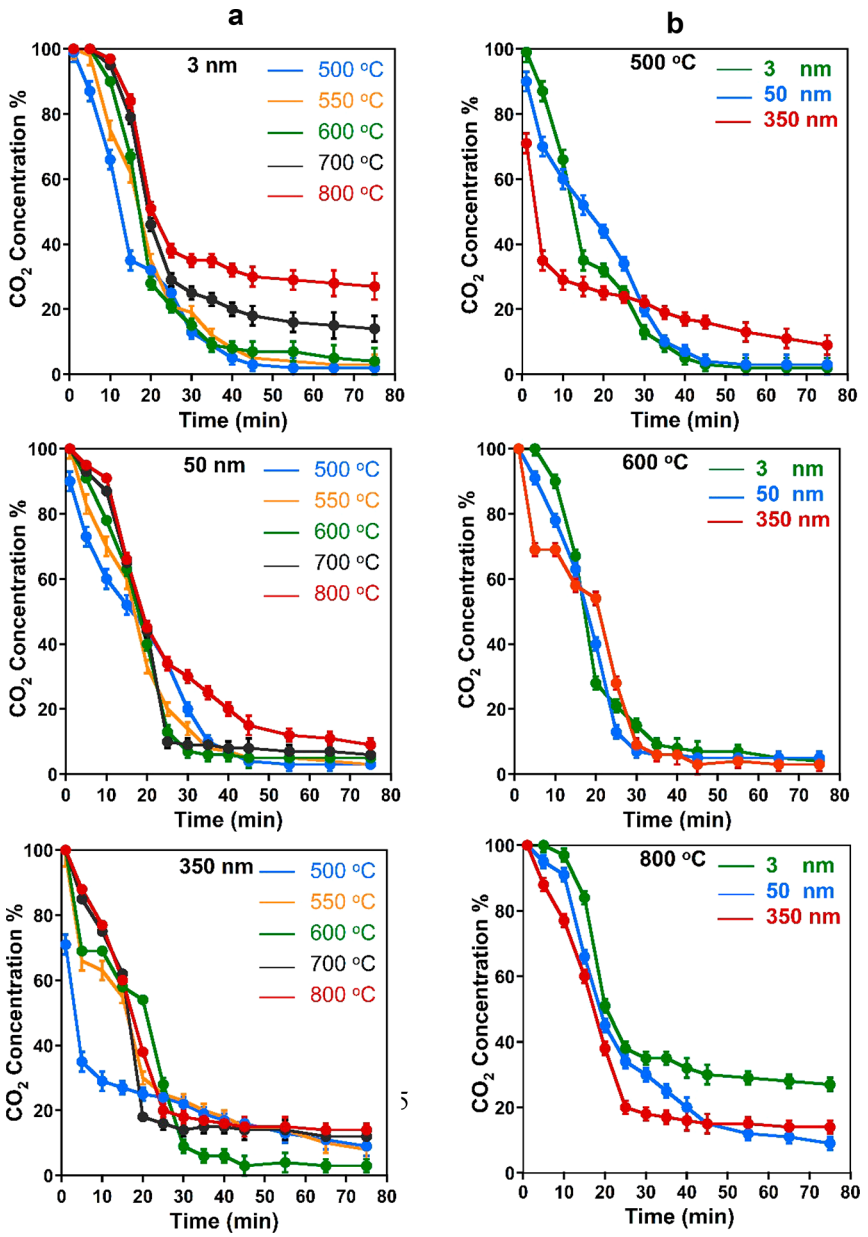


**Figure 3.** Effect of (a) temperature (500−800 °C) at a fixed particle size and (b) particle size at a fixed temperature on effluent $CO_2$ concentrations produced via $\alpha$-$Fe_2O_3$ oxidation of $CH_4$ (present at 5% in a standard P5 gas mixture) at a flow rate of 20 sccm (125 $h^{-1}$ as GHSV). Results from at least duplicate reactions are shown (as averages with standard deviation) for all concentration data.

Theoretical mass balance calculations were used to estimate the expected duration of full conversion of $CH_4$ to $CO_2$ (as well as $H_2O$) assuming lattice oxygen was available only through the reduction of $\alpha$-$Fe_2O_3$ to $Fe_3O_4$ (and not subsequent reduction of $Fe_3O_4$ or FeO). Based on these calculations, 100% conversion to $CO_2$ is estimated to last for approximately 90 min at a $CH_4$ flow rate of 2 sccm. For 3 nm particles at the highest temperature investigated (800 °C), $\alpha$-$Fe_2O_3$ performance nearly matched this theoretical estimate (85 (± 5) min). At all other reaction conditions, $\alpha$-$Fe_2O_3$ particles underperformed theoretical performance expectations, particularly with increasing primary particle size. We note, however, that even though 3 nm hematite particles were able to successfully achieve 100% conversion of $CH_4$ under these conditions, the amount of available oxygen utilized was very low (3% of total oxygen available), which would likely limit their effectiveness in real CLC applications.

The observed size-dependent trends for the duration of near-complete $CH_4$ to $CO_2$ conversion likely reflect the greater availability of lattice oxygen in smaller $\alpha$-$Fe_2O_3$ particles for $CH_4$ oxidation. As particle size decreases (from 350 to 3 nm), specific surface area increases while the volume of individual $\alpha$-$Fe_2O_3$ particles decreases. Accordingly, one might expect greater and easier access to lattice oxygen in smaller nanoparticles, especially if surface, rather than bulk, oxygen sites are responsible for controlling the rate of $CH_4$ oxidation (e.g., the unreacted shrinking core model).

Eventually, $CH_4$ breakthrough in the reactor effluent was observed for all particle sizes and at all temperatures. Breakthrough of $CH_4$ occurred concomitantly with a decrease in effluent $CO_2$ concentration, consistent with a loss in oxygen


DOI: 10.1021/acs.energyfuels.8b01539
Energy Fuels XXXX, XXX, XXX−XXX

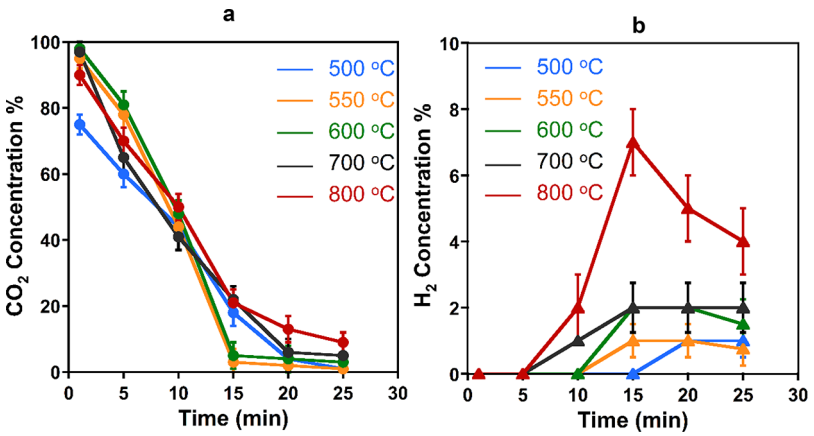


**Figure 4.** Concentration profiles (as %) of (a) $CO_2$ and (b) $H_2$ as a function of temperature (500−800 °C) during the reaction of 50 nm $\alpha$-$Fe_2O_3$ with $CH_4$ (present at 5% in a standard P5 gas mixture) at a flow rate of 40 sccm (250 $h^{-1}$ as GHSV). Results from at least duplicate reactions are shown (as averages with standard deviation) for all concentration data.

carrier performance. At the relatively low flow rate of 2 sccm, however, we never observed complete exhaustion of any oxygen carrier over the entire 160 min reaction, with some level of $CO_2$ always detected in the effluent (i.e., effluent $CH_4$ concentration was always below the influent $CH_4$ level). As with the duration of complete conversion to $CO_2$, the extent of $CH_4$ breakthrough also corresponded to $\alpha$-$Fe_2O_3$ particle size; the highest $CH_4$ effluent concentrations were observed for 350 nm particles, and the lowest for 3 nm particles, at all temperatures.

Finally, for the period where effluent $CO_2$ concentrations decrease steadily over time, we attribute the slower yet sustained conversion of $CH_4$ to an increasingly greater role for less reactive iron oxides generated through $\alpha$-$Fe_2O_3$ reduction (e.g., $Fe_3O_4$ and FeO) as oxygen carriers. Indeed, the activation energy required to extract the lattice oxygen of $Fe_3O_4$ or FeO is higher than that required for $\alpha$-$Fe_2O_3$.[41] Accordingly, the greater and more sustained production of $CO_2$ at higher temperatures most likely reflects the ability to more easily reduce $Fe_3O_4$ and/or FeO at these higher temperatures, in turn releasing their lattice oxygen to drive $CH_4$ oxidation.

**3.3. Flow Rate-Dependent Trends in $CH_4$ Oxidation by Nanoscale $\alpha$-$Fe_2O_3$.** *3.3.1. $CH_4$ Oxidation by $\alpha$-$Fe_2O_3$ at 20 sccm.* Figure 3 illustrates the performance of different $\alpha$-$Fe_2O_3$ particle sizes over the same temperature range (500−800 °C) but at the higher flow rate of 20 sccm (125 $h^{-1}$ as GHSV). As in Figure 2, data are shown as a function of temperature for each particle size (Figure 3a) and also as a function of particle size at each of the different temperature investigated (Figure 3b).

At this higher flow rate, as might be anticipated, the interval over which $CH_4$ was oxidized completely to $CO_2$ decreased considerably. For example, if we examine the performance of 3 nm $\alpha$-$Fe_2O_3$ particles at 800 °C, the interval of complete $CH_4$ conversion to $CO_2$ decreased from 85 (± 5) minutes at 2 sccm to 6 (± 2) minutes at 20 sccm (a change from 12.5 to 125 $h^{-1}$ as GHSV). While shorter in duration, estimates of full $CH_4$ conversion at this higher flow rate suggest that 3 nm particles still perform close to theoretical expectations based on the oxygen available from $\alpha$-$Fe_2O_3$ reduction to $Fe_3O_4$. Also, as shown in Figure 3b, the aforementioned trends in $\alpha$-$Fe_2O_3$ performance as a function of particle size were generally maintained at higher flow; $CH_4$ oxidation was still greatest in magnitude and sustained over the longest durations for smaller particles at higher temperatures.

Unlike at the lower flow rate shown in Figure 2, most reaction conditions resulted in near-complete or total exhaustion of oxygen carrier reactivity, with $CO_2$ effluent concentrations often reaching zero over longer time scales (typically greater than 30 min). For 3 nm particles, for example, the initial period of complete $CH_4$ conversion to $CO_2$ was followed by a period of steep activity loss where $CO_2$ concentration decreased rapidly over a relatively short period of time. At lower temperatures, effluent $CO_2$ concentration ultimately reached zero, although greater and more sustained effluent $CO_2$ levels were achieved at higher temperatures. This characteristic sigmoidal shape of effluent $CO_2$ profiles was also observed with the larger $\alpha$-$Fe_2O_3$ particles.

Experiments conducted at 20 sccm revealed important similarities in the rate of oxygen carrier reactivity loss along the reaction coordinate in $\alpha$-$Fe_2O_3$ systems. As shown in Figure 3a, the rate of 3 nm $\alpha$-$Fe_2O_3$ reactivity loss (based on the decrease in effluent $CO_2$ concentration over time) was practically invariant with temperature from 500 to 800 °C. This comparable rate of oxygen carrier reactivity loss is most easily discerned via semi-log plots of $CO_2$ concentration (as %) over time (Figure S4a). The linear portions of these plots suggest that oxygen carrier reactivity loss can be described as a first order process, where the slopes represent effective coefficients for reactivity loss. Accordingly, the near-equivalence of these slopes across all temperatures in Figure S4a illustrates the comparable rate of reactivity loss in the 3 nm $\alpha$-$Fe_2O_3$ systems. This behavior was also generally observed for 50 and 350 nm particles, where the rate of decrease in $CO_2$ yield over time was roughly constant over the temperatures investigated, with the exception of a distinct concentration profile for 350 nm particles at 500 °C. Moreover, as shown in Figure 3b, the rate of reactivity loss also appears to be roughly comparable across particle sizes at a given temperature. This is most clearly seen at higher temperatures (i.e., 600 and 800 °C), where the decrease in $CO_2$ concentration over time is nearly equivalent for 3, 50, and 350 nm particles (see Figure S4b which compares the semi-log plots of $CO_2$ effluent concentration over time for these systems at 2 sccm).

The relative independence of reactivity loss to both temperature and oxygen carrier particle size lends some insight into the reaction steps that are likely rate limiting in this



DOI: 10.1021/acs.energyfuels.8b01539
Energy Fuels XXXX, XXX, XXX−XXX

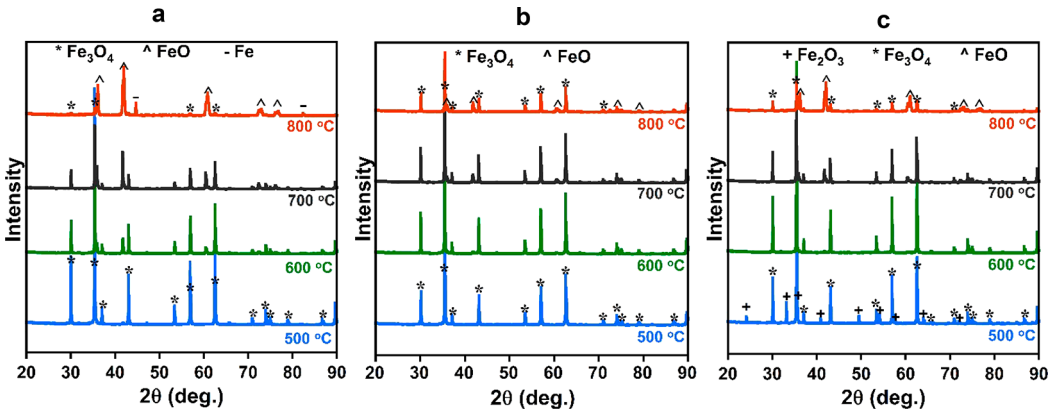


**Figure 5.** X-ray diffraction patterns for samples of (a) 3 nm, (b) 50 nm, and (c) 350 nm $\alpha$-$Fe_2O_3$ after 75 min of reaction with $CH_4$ (present at 5% in a standard P5 gas mixture) at 20 sccm. XRD patterns are shown for different reaction temperatures.

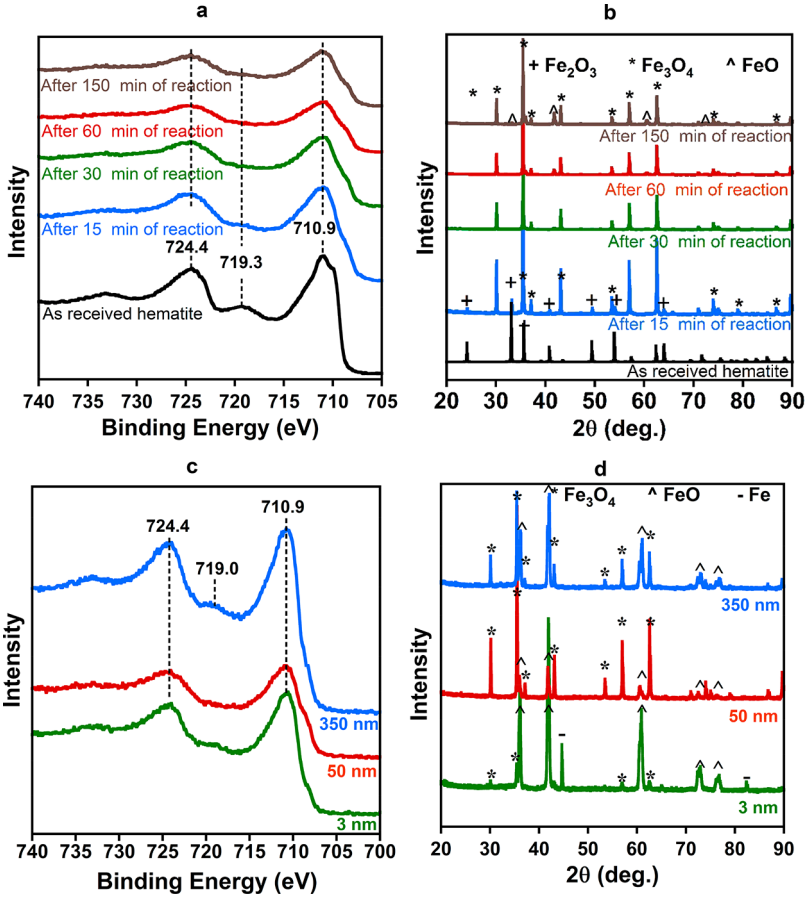


**Figure 6.** (a) XPS and (b) XRD of 50 nm $\alpha$-$Fe_2O_3$ as a function of reaction time with $CH_4$ (present at 5% in a standard P5 gas mixture) at 700 °C and 20 sccm. (c) XPS and (d) XRD of 3, 50, and 350 nm $\alpha$-$Fe_2O_3$ samples after reaction with P5 mixture at 800 °C and 20 sccm (GHSV = 125 $h^{-1}$) for 75 min.

performance regime. Factors like diffusion of reactants to (or products away from) the particle surface would be expected to scale with reactive surface area, which is a function of particle size. Thus, it is unlikely such physical processes control activity loss. Likewise, extraction of lattice oxygen and subsequent lattice rearrangement from $\alpha$-$Fe_2O_3$ to its reduction product $Fe_3O_4$ (or $Fe_3O_4$ to FeO) would also be expected to reveal a temperature dependence.[41] Thus, we interpret the size- and temperature-independent nature of reactivity loss as evidence that a process such as electron transfer, which classically exhibits little dependence on temperature, as rate limiting and responsible for reactivity loss in this regime.

In higher flow rate systems, we also observed formation of the partial oxidation products $H_2$ and CO (see eq 2) over longer time scales. Figure S5 shows the evolution of $H_2$ concentration over time both as a function of temperature for each particle size (Figure S5a) and as a function of particle size at a fixed temperature (Figure S5b) for systems with a flow rate of 20 sccm (GHSV of 125 $h^{-1}$). The extent of $H_2$ production was temperature dependent, with little to no $H_2$


DOI: 10.1021/acs.energyfuels.8b01539
Energy Fuels XXXX, XXX, XXX−XXX

(or CO) observed at the lowest temperature explored (500 °C). Although not shown, measured CO concentrations were half that quantified for $H_2$, as expected from the reaction stoichiometry in eq 2. While formation of $H_2$ and CO increased with temperature, there was only a weak dependence on particle size, with smaller $\alpha$-$Fe_2O_3$ particle sizes producing slightly higher $H_2$ and CO effluent levels at all temperatures.

*3.3.2. $CH_4$ Oxidation by $\alpha$-$Fe_2O_3$ at 40 sccm.* Oxygen carrier performance was also considered at an even higher $CH_4$ flow rate of 40 sccm (250 $h^{-1}$ GHSV), but these conditions revealed reactivity trends largely consistent with those established at lower flows. Figure 4 shows results from experiments with 50 nm $\alpha$-$Fe_2O_3$ particles at 40 sccm, specifically concentration profiles for effluent $CO_2$ (Figure 4a) and $H_2$ (Figure 4b) as a function of time. As illustrated in Figure 4a, oxygen carrier performance, both initially and over time, was relatively insensitive to temperature. Although the duration of near-complete $CH_4$ conversion to $CO_2$ was very short in all cases (~2 min), initial yields of $CO_2$ were roughly equivalent across the temperature range from 550 to 800 °C. This temperature independence may make $\alpha$-$Fe_2O_3$ nanoparticles promising oxygen carriers when hydrocarbon combustion at lower operating temperatures is desired.

Formation of partial combustions products CO and $H_2$ was also observed at this highest flow rate. Although CO and $H_2$ production occurred sooner than observed at 20 sccm, both products were formed to a lesser extent under these conditions. Notably, the concentration of $H_2$ was double that of CO, consistent with $H_2$ formation not resulting from $CH_4$ pyrolysis (eq 3), a process that can be promoted by Fe metal.[42]

$$CH_4 \rightarrow C + 2H_2 \quad (3)$$

**3.4. XPS and XRD Investigation of Solid-State $\alpha$-$Fe_2O_3$ Reduction Mechanism.** Figure 5 shows XRD patterns collected after 75 min of reaction between $\alpha$-$Fe_2O_3$ and $CH_4$ across the range of temperatures investigated. In all cases, the XRD patterns reveal that $CH_4$ oxidation to $CO_2$ is coupled with $\alpha$-$Fe_2O_3$ reduction to $Fe_3O_4$. Moreover, subsequent reduction of $Fe_3O_4$ to FeO, as well as FeO to Fe metal, was occasionally observed, but the extent of these reactions was temperature and particle size dependent. For example, while XRD diffraction lines indicative of $\alpha$-$Fe_2O_3$ remained detectable after 75 min of reaction for 350 nm particles at lower temperatures (e.g., 500 °C), $\alpha$-$Fe_2O_3$ was not detectable in reacted 3 nm particles at any temperature. Moreover, evidence of FeO and Fe metal from XRD was observed more readily for smaller particles (e.g., 3 nm) and at higher reaction temperatures (e.g., 800 °C). In fact, Fe metal was detected only in the 3 nm samples, suggesting that smaller $\alpha$-$Fe_2O_3$ particle size facilitates more complete reduction, consistent with our earlier assertion that lattice oxygen is more freely available and accessible in smaller particle sizes.

To examine differences between the bulk and surface chemical transformation of $\alpha$-$Fe_2O_3$ during reduction by $CH_4$, experiments with 50 nm $\alpha$-$Fe_2O_3$ (at 700 °C and 125 $h^{-1}$) were performed for different durations (15, 30, 45, 50, and 150 min), and the reacted oxygen carriers were analyzed by both XPS and XRD (corresponding to performance data in Figure 3). The high-resolution scan of the Fe 2p binding energy region (Figure 6a) shows two peaks at a binding energy of 710.9 and 724.4 assigned to $2p_{3/2}$ and $2p_{1/2}$ (of multiple iron oxides), respectively. However, the satellite structure (at 719.3 eV) unique to $\alpha$-$Fe_2O_3$[43,44] was not evident in XPS spectra for all reacted samples, suggesting a relatively rapid depletion of $\alpha$-$Fe_2O_3$ at the particle surface, even after just 15 min of reaction (at which point the $CO_2$ yield in the reactor effluent was ~65%). In contrast, complementary XRD patterns characterizing the bulk of these same samples (Figure 6b) revealed the persistence of $\alpha$-$Fe_2O_3$, at least through the sample collected after 15 min of reaction.

Over the duration of reaction, a shoulder grew at lower binding energies relative to the as-received $\alpha$-$Fe_2O_3$. XPS spectra, therefore, are consistent with the formation of reduced, ferrous iron species on the particle surface, such as $Fe_3O_4$ and FeO (with characteristic binding energies of 710.6 and 709.7 eV, respectively).[45,46] However, a reported satellite structure unique to FeO at 719.0 eV[44] does not appear in any of the XPS scans collected up to 150 min of reaction (i.e., well after oxygen carrier capacity is exceeded and the effluent $CO_2$ level is zero). While FeO does not appear present on the reacted particle surface, XRD analysis indicates its formation in the particle bulk over time, with diagnostic diffraction lines of FeO visible in the diffraction pattern collected after 150 min of reaction.

Additionally, we also conducted surface (XPS) and bulk (XRD) analysis of samples for each particle size (3, 50, and 350 nm) after reaction at 800 °C and 125 $h^{-1}$ for 75 min (Figure 6c and 6d, respectively), corresponding to the performance indicated by the last data point in Figure 3. A noteworthy observation involves the solid-state reduction of the 3 nm sample, which was the only material to produce an XRD pattern consistent with metallic iron formation (generated from the reduction of FeO). In contrast, corresponding surface analysis of the reacted samples did not reveal evidence for Fe metal formation on the particle surface, which would be expected to produce an XPS feature near a binding energy of 706.4.[46,47] Thus, formation of Fe metal was limited solely to the bulk, but not to the surface, of 3 nm particles, which after 75 min of reaction was still able to generate a $CO_2$ yield of roughly 30% in the reactor effluent.

Integrated surface and bulk chemical analysis allows us to elucidate the prevailing solid-state reduction mechanisms at play during $CH_4$ oxidation. The rapid surface depletion of $\alpha$-$Fe_2O_3$, along with its greater persistence in the particle bulk, is evidence that $\alpha$-$Fe_2O_3$ reduction to $Fe_3O_4$ proceeds in a matter consistent with the unreacted shrinking core model (USCM).[25] Thus, $CH_4$ oxidation is initiated by the surface oxygen of $\alpha$-$Fe_2O_3$. Once a thin layer of the reduced iron oxide phase (i.e., magnetite, $Fe_3O_4$) is formed on the particle surface, further oxidation of $CH_4$ molecules can occur only after they diffuse through the reduced layer to access and react with the underlying, bulk oxygen molecules.[24,41,48] According to this model, $\alpha$-$Fe_2O_3$ particle size would be expected to influence performance, as we observed; larger surface area to volume ratios would not only provide more surface oxygen per particle to initiate reaction but also allow for a smaller diffusion length (and thus resistance) for $CH_4$ to access the underlying, unreacted particle core as the reaction proceeds.

In an important distinction, our characterization suggests an alternative solid-state reduction mechanism for the products of $\alpha$-$Fe_2O_3$ reduction. Specifically, after $\alpha$-$Fe_2O_3$ conversion to $Fe_3O_4$ following the unreacted shrinking core model, characterization data suggest that subsequent conversion of $Fe_3O_4$ to FeO (and in the case of 3 nm particles, FeO to iron metal) proceeds via the nucleation and nuclei growth model (NNGM), as we have reported previously for cobalt oxides.[22]



DOI: 10.1021/acs.energyfuels.8b01539
Energy Fuels XXXX, XXX, XXX−XXX

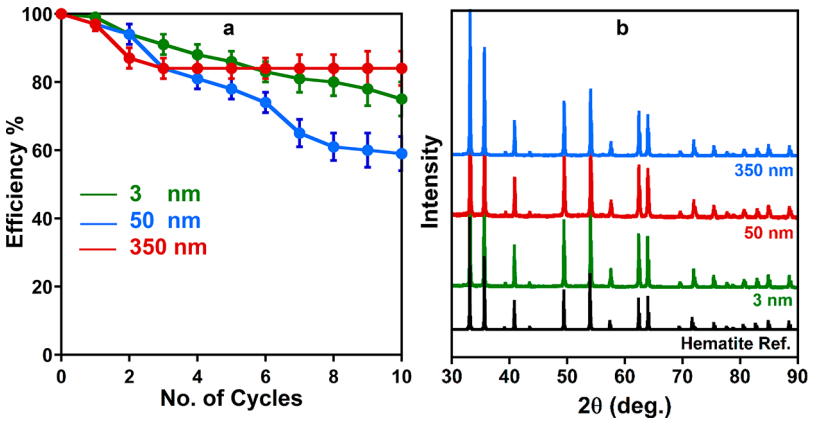


**Figure 7.** (a) Oxygen carrier efficiency of 3, 50, and 350 nm $\alpha$-$Fe_2O_3$ samples across 10 cycles of reduction by P5 gas (20 sccm, 5 min reaction time) followed by reoxidation in air (60 sccm, 5 min reaction time) at 600 °C. (b) XRD patterns of oxygen carriers after 10 complete P5 reduction−air oxidation cycles.

When $Fe_3O_4$ is the predominant iron phase, integrated characterization indicates that particle surfaces stay enriched in more heavily oxidized phases, while more reduced phases are readily detected in the bulk. In this scenario, bulk oxygen from $Fe_3O_4$ and FeO migrates to the particle surface, where the heterogeneous reaction with $CH_4$ occurs. Methane oxidation results in the formation of oxygen vacancies on the particle surface, which in turn drives migration of bulk oxygen to the surface via an electron transfer process we earlier proposed as rate limiting and relatively insensitive to particle size. This oxygen migration is responsible for maintaining the higher oxidation state of iron atoms at the particle surface relative to the more reduced oxidation state in the bulk. Ultimately, this solid-state reduction scheme, where the more reduced phase transitions from surface-to-bulk ("outside in") to bulk-to-surface ("inside out") along the reaction coordinate from $\alpha$-$Fe_2O_3$ to $Fe_3O_4$, FeO, and finally iron metal, agrees well with mechanisms previously proposed, but not experimentally verified with integrated bulk and surface characterization, by Monazam and co-workers.[23,24]

As a final line of evidence, XPS analysis of the oxygen region (Figure S6a) generally supports our hypothesized reduction mechanism. The surface oxygen concentration decreased with reaction progress, which matches expectations for transformation of $\alpha$-$Fe_2O_3$ to $Fe_3O_4$ and the further reduction to FeO. XPS analysis of the carbon region (Figure F6b) revealed an increase in surface carbon concentration over time, which is expected from the deposition of carbon on the oxygen carrier surface as a by-product of reaction.

**3.5. Practical Performance Considerations for Nanoparticle Oxygen Carriers.** The successful use of nanoparticles as oxygen carriers in CLC must overcome practical challenges related to their application, including agglomeration, which causes structural changes (e.g., loss of surface area and increase in particle volume) that can adversely affect performance. We conducted additional tests to explore the practical viability of unsupported $\alpha$-$Fe_2O_3$ nanoparticles during simulated CLC cycling and the influence of agglomeration on the long-term performance of $\alpha$-$Fe_2O_3$ nanoparticles.

Figure 7a considers oxygen carrier efficiency across ten sequential reduction/oxidation cycles, where we define oxygen carrier efficiency as the ratio of the $CO_2$ yield at the end of each reduction cycle (5 min) to the $CO_2$ yield measured at the end of the first cycle (expressed as %). Generally, under these conditions (600 °C; reduction with P5 at flow rate of 20 sccm; reoxidation with air at 60 sccm; each reaction time of 5 min) $\alpha$-$Fe_2O_3$ nanoparticles exhibited reversible reduction/oxidation through all 10 CLC cycles, with XRD analysis confirming that reoxidation of used samples after ten cycles resulted in $\alpha$-$Fe_2O_3$ regeneration (Figure 7b). However, a gradual loss in performance was observed through the 10 cycles, a trend most prominent for 50 and 3 nm particles (Figure 7a). After 10 reduction−oxidation cycles, the reactivity of the 3 and 50 nm samples dropped by roughly 25% and 40%, respectively, relative to pristine materials. While the 350 nm sample had a sharp initial drop in efficiency (decreasing 15% over the first 4 cycles), it exhibited more sustained performance for the remainder of the cycling experiment.

We attribute this behavior to the tendency of the smallest nanoparticles (3 and 50 nm) to more readily agglomerate at high reaction temperatures, thereby hindering their long-term, sustained performance. Indeed, SEM analysis of the oxygen carrier samples after ten complete reaction cycles reveals that 3, 50, and 350 nm samples grow to 90 (± 20), 400 (± 150), and 450 (± 180) nm, respectively (see Figure S7). Thus, while smaller nanoparticles exhibit superior performance during a single reduction cycle (see Figure 2), their tendency to agglomerate may limit such size-dependent reactivity benefits over repeated oxygen carrier cycling in CLC.

**3.6. Atomistic Thermodynamics Analysis of $FeO_x$ Bulk and Surface Species.** DFT and thermodynamics modeling were carried out to determine if there is a driving force for the crossover from USCM to NNGM reduction mechanisms. To this end, (001) surface models representing partially reduced $\alpha$-$Fe_2O_3$ were generated, starting from the ideal surface and then introducing oxygen vacancies in the outermost oxygen layers. By employing varying sized supercells, different oxygen vacancy densities can be described within the structurally periodic models. Details of the surface model construction are given in Figure S8 of the Supporting Information. In addition to the ideal $\alpha$-$Fe_2O_3$(001), three surface models were designed. The 25% oxygen vacancy surface is terminated by 3 (1 × 1) domains of $Fe_2O_3$ and 1 (1 × 1) domain of $Fe_2O_2$, which is equivalent in chemical formula to a stoichiometry of 2/3 $Fe_3O_4$ + 1/3 $Fe_2O_3$. In a similar fashion, the 50% oxygen vacancy structure is terminated by 2 (1 × 1) domains of $Fe_2O_3$ and 2 (1 × 1) domains of $Fe_2O_2$, which is equivalent in chemical


DOI: 10.1021/acs.energyfuels.8b01539
Energy Fuels XXXX, XXX, XXX−XXX

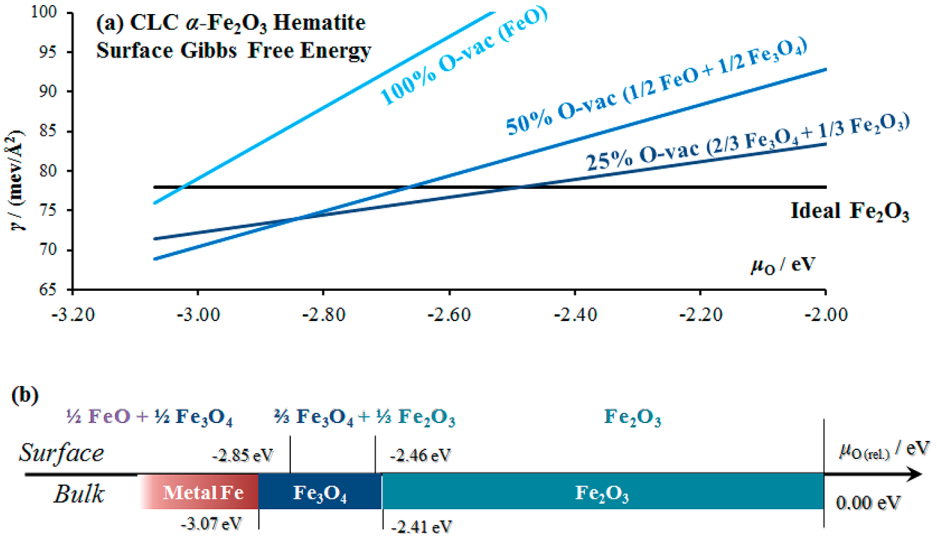


**Figure 8.** Results of surface and bulk atomistic thermodynamics analysis. (a) Surface free energy ($\gamma$) as a function of oxygen chemical potential, $\mu_O$, for FeOx species ranging from $\alpha$-$Fe_2O_3$ to FeO, and (b) comparison of surface (upper) and bulk (lower) stability ranges as a function of $\mu_O$.

formula to a stoichiometry of 1/2 FeO + 1/2 $Fe_3O_4$. The 100% surface oxygen vacancy model is comprised of FeO in a (1 × 1) cell.

Results of the ab initio thermodynamics analysis of the surface and bulk FeOx species are summarized in Figure 8. The plot in Figure 8a shows the calculated values of the surface free energy ($\gamma$) of the corresponding hematite surface at different values of oxygen chemical potential ($\mu_O$). The O-rich limit ($\mu_O$ = 0) is defined as a gas-phase equilibrium, and the O-poor limit ($\mu_O$ = −3.07 eV) is defined by bulk equilibrium, following previous work.[34] The plot of $\gamma$ shows that when $\mu_O$ is > −2.46 eV, the ideal Fe-terminated surface is most stable. For $\mu_O$ in the range of −2.85 to −2.46 eV, the 2/3 $Fe_3O_4$ + 1/3 $Fe_2O_3$ surface stoichiometry is predicted to be the most stable. When $\mu_O$ is even lower, the more reduced surface with 1/2 FeO + 1/2 $Fe_3O_4$ stoichiometry becomes preferred. In Figure 8b the stability ranges for the variable surface stoichiometries are compared to calculated regions of variable bulk $FeO_x$ stability. The stable region of bulk $\alpha$-$Fe_2O_3$ corresponds to values of $\mu_O$ down to −2.41 eV. In the region of −3.07 to −2.41 eV bulk $Fe_3O_4$ is preferred, and below −3.07 eV the bulk iron oxide is predicted to be fully reduced to metallic Fe.

The fact that there is a narrow window of overlap between bulk $\alpha$-$Fe_2O_3$ and the (2/3 $Fe_3O_4$ + 1/3 $Fe_2O_3$) surface supports that reduced ($Fe_3O_4$) layers are stable over $Fe_2O_3$ cores. This theoretical result is congruent with the experimental evidence that reduction of $\alpha$-$Fe_2O_3$ proceeds initially through the USCM mechanism. On the other hand, the relatively high values of $\gamma$ for the FeO surface over the full range of $\mu_O$ suggests that the hematite core would decompose before shells of this reduced form would form. The absence of overlapping regions of stability of bulk $\alpha$-$Fe_2O_3$ and FeO surfaces along the $\mu_O$ axis is in agreement with the crossover from USCM to NNGM over the course of nanoparticle reduction. We note that our calculations were limited to geometries based on $\alpha$-$Fe_2O_3$(001) surfaces, at relatively high oxygen density concentrations. Therefore, we consider the theoretical modeling to be supportive, but not definitively conclusive evidence, of the two-stage USCM/NNGM reduction of the experimental nanoparticles.

## 4. CONCLUSION

For the oxidation of $CH_4$ by $\alpha$-$Fe_2O_3$ during the CLC process, we observed that decreasing the particle size from 350 to 3 nm increased the duration over which $CH_4$ was completely converted to $CO_2$. We attribute this size-dependent performance trend to a greater availability of lattice oxygen in $\alpha$-$Fe_2O_3$ nanoparticles that possess a high surface area to volume ratio. After the period of complete $CH_4$ conversion, all particle sizes exhibited a relatively steep decline in performance. Notably, the rate of reactivity loss was roughly constant across the temperatures and particle sizes considered. The lower reactivity reflects, in part, a depletion of $\alpha$-$Fe_2O_3$ and a greater role for $Fe_3O_4$, its less reactive reduction product, in $CH_4$ oxidation. Further, the relative independence of reactivity loss on particle size and temperature leads us to propose that the rate-determining step is likely electron transfer, which would exhibit little to no temperature dependence. More practically, the relative insensitivity of $\alpha$-$Fe_2O_3$ nanoparticle performance from 500 to 800 °C highlights its potential as an oxygen carrier at lower, less energy intensive reactor temperatures.

Using integrated bulk (XRD) and surface (XPS) characterization, we propose that $\alpha$-$Fe_2O_3$ reduction to $Fe_3O_4$ is best described by the unreacted shrinking core model (USCM), where the reduced phase is enriched at the particle surface relative to the oxidized particle bulk. We also propose that the subsequent reduction of $Fe_3O_4$ to FeO, as well as the further reduction of FeO to Fe metal, follows the nucleation and nuclei growth model (NNGM). This two-stage mechanism of oxygen carrier reduction is in good agreement with mechanisms previously proposed, but not verified with materials characterization, for $\alpha$-$Fe_2O_3$ reduction.[23,24] Our ab initio thermodynamics analysis of $FeO_x$ bulk and surface species also provides theoretical support of this two-stage mechanism. While partially reduced $\alpha$-$Fe_2O_3$ surfaces have predicted stability over a portion of the same range of oxygen chemical potentials under which bulk $\alpha$-$Fe_2O_3$ is stable, the calculations predict that hematite would fully decompose before surfaces of FeO would be stable as outer layers.

Ultimately, our investigation provides evidence to support conventional wisdom[25] that decreasing oxygen carrier particle size can be used to improve performance. However, any gains


DOI: 10.1021/acs.energyfuels.8b01539
Energy Fuels XXXX, XXX, XXX−XXX

in performance achieved with nanoparticles must overcome their somewhat inferior mechanical properties that may affect their performance and stability during extended CLC cycling.[30] A solution for these issues could be the use of an appropriate support for the nanoparticles, which would limit agglomeration while maximizing those properties (i.e., high surface area and small particle volume) most beneficial for increasing availability and accessibility of lattice oxygen.

## ■ ASSOCIATED CONTENT

### Supporting Information

The Supporting Information is available free of charge on the ACS Publications website at DOI: 10.1021/acs.energyfuels.8b01539.

Schematic of flow through reactor system, additional characterization and performance results, and theoretical yield calculations (PDF)

## ■ AUTHOR INFORMATION


### Corresponding Authors

*E-mail: david-cwiertny@uiowa.edu. Tel.: 319.335.1401. Address: 4655 Seamans Center, Iowa City, IA 52242, United States.

*E-mail: vhgrassian@ucsd.edu. Tel.: (858) 534-4159. Address: University of California San Diego, 9500 Gilman Drive, Mail Code 0314, La Jolla, CA 92093, United States.

### ORCID

Vicki H. Grassian: 0000-0001-5052-0045

David M. Cwiertny: 0000-0001-6161-731X


### Notes

The authors declare no competing financial interest.

## ■ ACKNOWLEDGMENTS

The authors acknowledge support from the National Science Foundation (CBET-1509432). H.A. acknowledges support from The Higher Committee for Education Development in Iraq (HCED) and the Middle Technical University (MTU). S.E.M. acknowledges Dr. Xu Huang for carrying out DFT calculations and preparing figures related to the theoretical modeling. This research was supported in part through computational resources provided by the University of Iowa, Iowa City, Iowa. This work used the Extreme Science and Engineering Discovery Environment (XSEDE[49]), which is supported by the National Science Foundation (ACI-1548562). We also acknowledge the helpful comments of three anonymous reviewers whose input improved the clarity and strength of this work.

## ■ REFERENCES


(1) Kwak, B. S.; Park, N. K.; Baek, J. I.; Ryu, H. J.; Kang, M. Improvement of reduction and oxidation performance of MMgOx (M = Fe, Co, Ni, and Cu) particles for chemical looping combustion. *Powder Technol.* **2017**, *312*, 237−247.

(2) Su, M. Z.; Zhao, H. B.; Tian, X.; Zhang, P. F.; Du, B. Z.; Liu, Z. G. Intrinsic reduction kinetics investigation on a hematite oxygen carrier by CO in chemical looping combustion. *Energy Fuels* **2017**, *31*, 3010−3018.

(3) Huang, W. C.; Kuo, Y. L.; Su, Y. M.; Tseng, Y. H.; Lee, H. Y.; Ku, Y. A facile method for sodium-modified $Fe_2O_3/Al_2O_3$ oxygen carrier by an air atmospheric pressure plasma jet for chemical looping combustion process. *Chem. Eng. J.* **2017**, *316*, 15−23.

(4) Ma, J. C.; Tian, X.; Zhao, H. B.; Bhattacharya, S.; Rajendran, S.; Zheng, C. G. Investigation of two hematites as oxygen carrier and two low-rank coals as fuel in chemical looping combustion. *Energy Fuels* **2017**, *31*, 1896−1903.

(5) Breault, R. W.; Monazam, E. R. Modeling of the reduction of hematite in the chemical looping combustion of methane using barracuda. *Energy Technology* **2016**, *4*, 1221−1229.

(6) Hua, X. N.; Wang, W.; Wang, F. Performance and kinetics of iron-based oxygen carriers reduced by carbon monoxide for chemical looping combustion. *Front. Environ. Sci. Eng.* **2015**, *9*, 1130−1138.

(7) Hafizi, A.; Rahimpour, M. R.; Hassanajili, S. Hydrogen production via chemical looping steam methane reforming process: Effect of cerium and calcium promoters on the performance of Fe2O3/Al2O3 oxygen carrier. *Appl. Energy* **2016**, *165*, 685−694.

(8) Neal, L.; Shafiefarhood, A.; Li, F. X. Effect of core and shell compositions on MeOx@LaySr1-y$FeO_3$ core-shell redox catalysts for chemical looping reforming of methane. *Appl. Energy* **2015**, *157*, 391−398.

(9) Kang, D.; Lim, H. S.; Lee, M.; Lee, J. W. Syngas production on a Ni-enhanced $Fe_2O_3/Al_2O_3$ oxygen carrier via chemical looping partial oxidation with dry reforming of methane. *Appl. Energy* **2018**, *211*, 174−186.

(10) Hossain, M. M.; de lasa, H. I. Chemical-looping combustion (CLC) for inherent $CO_2$ separations-a review. *Chem. Eng. Sci.* **2008**, *63*, 4433−4451.

(11) Ketteler, G.; Weiss, W.; Ranke, W.; Schlögl, R. Bulk and surface phases of iron oxides in an oxygen and water atmosphere at low pressure. *Phys. Chem. Chem. Phys.* **2001**, *3*, 1114−1122.

(12) Yang, W. J.; Zhao, H. B.; Wang, K.; Zheng, C. G. Synergistic effects of mixtures of iron ores and copper ores as oxygen carriers in chemical-looping combustion. *Proc. Combust. Inst.* **2015**, *35*, 2811−2818.

(13) Jerndal, E.; Mattisson, T.; Lyngfelt, A. Thermal analysis of chemical-looping combustion. *Chemical Engineering Research & Design* **2006**, *84*, 795−806.

(14) Scott, S. A.; Dennis, J. S.; Hayhurst, A. N.; Brown, T. In situ gasification of a solid fuel and $CO_2$ separation using chemical looping. *AIChE J.* **2006**, *52*, 3325−3328.

(15) Tong, A.; Zeng, L.; Kathe, M. V.; Sridhar, D.; Fan, L.-S. Application of the moving-bed chemical looping process for high methane conversion. *Energy Fuels* **2013**, *27*, 4119−4128.

(16) Utigard, T. A.; Wu, M.; Plascencia, G.; Marin, T. Reduction kinetics of Goro nickel oxide using hydrogen. *Chem. Eng. Sci.* **2005**, *60*, 2061−2068.

(17) Richardson, J. T.; Scates, R. M.; Twigg, M. V. X-ray diffraction study of the hydrogen reduction of, NiO/alpha-$Al_2O_3$ steam reforming catalysts. *Appl. Catal., A* **2004**, *267*, 35−46.

(18) Son, S. R.; Kim, S. D. Chemical-looping combustion with NiO and $Fe_2O_3$ in a thermobalance and circulating fluidized bed reactor with double loops. *Ind. Eng. Chem. Res.* **2006**, *45*, 2689−2696.

(19) Levenspiel, O. Chemical reaction engineering. *Ind. Eng. Chem. Res.* **1999**, *38*, 4140−4143.

(20) Briggs, R. A.; Sacco, A. Hydrogen reduction-mechanisms of ilmenite between 823 and 1353-K. *J. Mater. Res.* **1991**, *6*, 574−584.

(21) Starink, M. J. On the meaning of the impingement parameter in kinetic equations for nucleation and growth reactions. *J. Mater. Sci.* **2001**, *36*, 4433−4441.

(22) Alalwan, H. A.; Cwiertny, D. M.; Grassian, V. H. $Co_3O_4$ nanoparticles as oxygen carriers for chemical looping combustion: A materials characterization approach to understanding oxygen carrier performance. *Chem. Eng. J.* **2017**, *319*, 279−287.

(23) Monazam, E. R.; Breault, R. W.; Siriwardane, R. Kinetics of hematite to wustite by hydrogen for chemical looping combustion. *Energy Fuels* **2014**, *28*, 5406−5414.

(24) Monazam, E. R.; Breault, R. W.; Siriwardane, R.; Richards, G.; Carpenter, S. Kinetics of the reduction of hematite ($Fe_2O_3$) by methane ($CH_4$) during chemical looping combustion: A global mechanism. *Chem. Eng. J.* **2013**, *232*, 478−487.

(25) Li, J.; Zhang, H. D.; Gao, Z. P.; Fu, J.; Ao, W. Y.; Dai, J. J. $CO_2$ capture with chemical looping combustion of gaseous fuels: An overview. *Energy Fuels* **2017**, *31*, 3475−3524.




DOI: 10.1021/acs.energyfuels.8b01539
*Energy Fuels* XXXX, XXX, XXX−XXX

(26) Rehmat, A.; Saxena, S. C. Single nonisothermal noncatalytic solid-gas reaction-effect of changing particle size. *Ind. Eng. Chem. Process Des. Dev.* **1976**, *15*, 343−350.
(27) Liu, Y.; Kirchesch, P.; Graule, T.; Liersch, A.; Clemens, F. Nanoparticle prepared mechanically stable hierarchically porous silica granulates and their application as oxygen carrier supports for chemical looping combustion. *J. Mater. Chem. A* **2015**, *3*, 11863−11873.
(28) Xu, Z. W.; Zhao, H. B.; Wei, Y. J.; Zheng, C. G. Self-assembly template combustion synthesis of a core-shell CuO@$TiO_2$-$Al_2O_3$ hierarchical structure as an oxygen carrier for the chemical-looping processes. *Combust. Flame* **2015**, *162*, 3030−3045.
(29) Pang, J. M.; Guo, P. M.; Zhao, P.; Cao, C. Z.; Zhang, D. W. Influence of Size of Hematite Powder on Its Reduction Kinetics by $H_2$ at Low Temperature. *J. Iron Steel Res. Int.* **2009**, *16*, 7−11.
(30) Wen, D.; Song, P.; Zhang, K.; Qian, J. Thermal oxidation of iron nanoparticles and its implication for chemical-looping combustion. *J. Chem. Technol. Biotechnol.* **2011**, *86*, 375−380.
(31) Giannozzi, P.; Baroni, S.; Bonini, N.; Calandra, M.; Car, R.; Cavazzoni, C.; Ceresoli, D.; Chiarotti, G.L.; Cococcioni, M.; Dabo, I. Quantum Espresso: A modular and open-source software project for quantum simulations of materials. *Journal of Physics-Condensed Matter* **2009**, *21*, 1.
(32) Perdew, J. P.; Burke, K.; Ernzerhof, M. Generalized gradient approximation made simple. *Phys. Rev. Lett.* **1996**, *77*, 3865−3868.
(33) Vanderbilt, D. Soft self-consistent pseudopotenials in a generalized eigenvalue formalism. *Phys. Rev. B: Condens. Matter Mater. Phys.* **1990**, *41*, 7892−7895.
(34) Monkhorst, H. J.; Pack, J. D. Special points for brillouin-zone integrations. *Phys. Rev. B* **1976**, *13*, 5188−5192.
(35) Huang, X.; Ramadugu, S. K.; Mason, S. E. Surface-specific DFT plus U approach applied to alpha-$Fe_2O_3$(0001). *J. Phys. Chem. C* **2016**, *120*, 4919−4930.
(36) Reuter, K.; Scheffler, M. Composition, structure, and stability of $RuO_2$ (110) as a function of oxygen pressure. *Phys. Rev. B: Condens. Matter Mater. Phys.* **2001**, *65*, 035406.
(37) Sun, Q.; Reuter, K.; Scheffler, M. Effect of a humid environment on the surface structure of $RuO_2$(110). *Phys. Rev. B: Condens. Matter Mater. Phys.* **2003**, *67*, 1.
(38) Reuter, K.; Scheffler, M. Composition and structure of the $RuO_2$ (110) surface in an $O_2$ and CO environment: Implications for the catalytic formation of $CO_2$. *Phys. Rev. B: Condens. Matter Mater. Phys.* **2003**, *68*, 045407.
(39) Trainor, T. P.; Chaka, A. M.; Eng, P. J.; Newville, M.; Waychunas, G. A.; Catalano, J. G.; Brown, G. E. Structure and reactivity of the hydrated hematite (0001) surface. *Surf. Sci.* **2004**, *573*, 204−224.
(40) Nguyen, M.T.; Seriani, N.; Gebauer, R. Water adsorption and dissociation on alpha-$Fe_2O_3$(0001): PBE+U calculations. *J. Chem. Phys.* **2013**, *138*, 194709.
(41) Breault, R. W.; Monazam, E. R. Analysis of fixed bed data for the extraction of a rate mechanism for the reaction of hematite with methane. *J. Ind. Eng. Chem.* **2015**, *29*, 87−96.
(42) Miller, D. D.; Siriwardane, R. Mechanism of methane chemical looping combustion with hematite promoted with $CeO_2$. *Energy Fuels* **2013**, *27*, 4087−4096.
(43) Muhler, M.; Schlogl, R.; Ertl, G. The nature of the iron oxide-based catalyst for dehydrogenation of ethylbenzene to styrene. *J. Catal.* **1992**, *138*, 413−444.
(44) Yamashita, T.; Hayes, P. Analysis of XPS spectra of $Fe^{2+}$ and $Fe^{3+}$ ions in oxide materials. *Appl. Surf. Sci.* **2008**, *254*, 2441−2449.
(45) Biesinger, M. C.; Payne, B. P.; Grosvenor, A. P.; Lau, L. W. M.; Gerson, A. R.; Smart, R. S. C. Resolving surface chemical states in XPS analysis of first row transition metals, oxides and hydroxides: Cr, Mn, Fe, Co and Ni. *Appl. Surf. Sci.* **2011**, *257*, 2717−2730.
(46) Hawn, D. D.; Dekoven, B. M. Deconvolution as a correction for photoelectron inelastic energy losses in the core level XPS spectra of iron oxides. *Surf. Interface Anal.* **1987**, *10*, 63−74.
(47) Biesinger, M. C.; Payne, B. P.; Grosvenor, A. P.; Lau, L. W. M.; Gerson, A. R.; Smart, R. S. Resolving surface chemical states in XPS analysis of first row transition metals, oxides and hydroxides: Cr, Mn, Fe, Co and Ni. *Appl. Surf. Sci.* **2011**, *257*, 2717−2730.
(48) Lu, X.; Rahman, R. A.; Lu, D. Y.; Ridha, F. N.; Duchesne, M. A.; Tan, Y.; Hughes, R. W. Pressurized chemical looping combustion with CO: Reduction reactivity and oxygen-transport capacity of ilmenite ore. *Appl. Energy* **2016**, *184*, 132−139.
(49) Towns, J.; Cockerill, T.; Dahan, M.; Foster, I.; Gaither, K.; Grimshaw, A.; Hazlewood, V.; Lathrop, S.; Lifka, D.; Peterson, G. D.; et al. XSEDE: Accelerating scientific discovery. *Comput. Sci. Eng.* **2014**, *16*, 62−74.


DOI: 10.1021/acs.energyfuels.8b01539
*Energy Fuels* XXXX, XXX, XXX−XXX